Zodiacal Exoplanets in Time (ZEIT). VIII. A Two-planet System in Praesepe from *K2* Campaign 16

Aaron C. Rizzuto[1,6] , Andrew Vanderburg[1,7] , Andrew W. Mann[2] , Adam L. Kraus[1] , Courtney D. Dressing[3] ,
Marcel A. Agüeros[4] , Stephanie T. Douglas[5,8] , and Daniel M. Krolikowski[1]
[1] Department of Astronomy, The University of Texas at Austin, Austin, TX 78712, USA; arizz@astro.as.utexas.edu
[2] Department of Physics and Astronomy, The University of North Carolina at Chapel Hill, Chapel Hill, NC 27599, USA
[3] Astronomy Department, University of California, Berkeley, CA 94720, USA
[4] Department of Astronomy, Columbia University, 550 West 120th Street, New York, NY 10027, USA
[5] Harvard-Smithsonian Center for Astrophysics, 60 Garden Street, Cambridge, MA 02138, USA

Abstract

Young planets offer a direct view of the formation and evolution processes that produced the diverse population of mature exoplanet systems known today. The repurposed *Kepler* mission *K2* is providing the first sample of young transiting planets by observing populations of stars in nearby, young clusters and stellar associations. We report the detection and confirmation of two planets transiting K2-264, an M2.5 dwarf in the 650 Myr old Praesepe open cluster. Using our notch-filter search method on the *K2* light curve, we identify planets with periods of 5.84 and 19.66 days. This is currently the second known multi-transit system in open clusters younger than 1 Gyr. The inner planet has a radius of $2.27^{+0.20}_{-0.16}\,R_\oplus$ and the outer planet has a radius of $2.77^{+0.20}_{-0.18}\,R_\oplus$. Both planets are likely mini-Neptunes. These planets are expected to produce radial velocity signals of 3.4 and 2.7 m s^{-1}, respectively, which is smaller than the expected stellar variability in the optical ($\simeq$30 m s^{-1}), making mass measurements unlikely in the optical but possible with future near-infrared spectrographs. We use an injection-recovery test to place robust limits on additional planets in the system and find that planets larger than $2\,R_\oplus$ with periods of 1–20 days are unlikely.

Key words: open clusters and associations: individual – planetary systems – planets and satellites: formation – stars: low-mass

1. Introduction

Planets and their host stars can change dramatically over their lifetimes. Their structural, orbital, and atmospheric properties are all expected to evolve through interactions with their host star (e.g., Ehrenreich et al. 2015), the protoplanetary disk from which they formed (e.g., Cloutier & Lin 2013), other planets in the system (e.g., Chatterjee et al. 2008), and the greater stellar environment (e.g., Cai et al. 2018). Understanding the underlying drivers and relative importance of these evolutionary mechanisms is critical for revealing the early sculpting of planetary systems and the conditions that give rise to the diversity of mature planetary systems revealed by *Kepler* and earlier exoplanet surveys (e.g., Lissauer et al. 2014; Inamdar & Schlichting 2016).

Exoplanets likely evolve the most during their first Gyr (e.g., Adams & Laughlin 2006; Mann et al. 2010; Lopez et al. 2012), and planets <1 Gyr old are therefore powerful probes of the important drivers of exoplanet evolution. Fortuitously, the repurposed *Kepler* mission, *K2* (Howell et al. 2014), has surveyed a number of young clusters and star-forming regions spanning <10 Myr (Taurus-Auriga; Kraus et al. 2017), to ≃650 Myr (Praesepe and Hyades; Martín et al. 2018), with

Upper Scorpius (≃10 Myr; Pecaut et al. 2012) and the Pleiades (≃112 Myr; Dahm 2015) spanning intermediate ages.

The Zodiacal Exoplanets in Time (ZEIT) survey (Mann et al. 2016a) was designed to identify and characterize transiting planets in these young clusters and star-forming regions using the precise photometry from *K2* (Van Cleve et al. 2016). The greater goal is to better understand how planets form and evolve by comparing the statistical properties of exoplanets of different ages and to older systems found during the original *Kepler* mission (Borucki et al. 2010; Thompson et al. 2018). Thus far we have identified planets in Hyades (Vanderburg et al. 2018), Praesepe (Mann et al. 2017b), and Upper Scorpius (Mann et al. 2016b), many of which were found near-simultaneously by similar surveys focusing on exoplanets in young stellar associations (e.g., David et al. 2016; Obermeier et al. 2016; Pepper et al. 2017; Ciardi et al. 2018; Livingston et al. 2018).

Multi-transiting planetary systems are uniquely useful for studying stellar and planetary properties. In cases where the planets' eccentricities can be independently constrained (e.g., through dynamics; Deck & Agol 2016; Gillon et al. 2017), multi-transiting systems can be used to constrain stellar densities with a precision that rivals eclipsing binaries (e.g., Mann et al. 2017a). Even with no information on the host star properties, differences between the measured transit duration of planets in the same system can be used to measure the relative eccentricities (Kipping et al. 2012). Multi-transit systems where planets undergo transit timing variations (TTVs) offer the best opportunity to measure the masses of small planets (e.g., Deck & Agol 2015; Hadden & Lithwick 2017). Lastly, these systems provide a measurement of the mutual inclination of planets, a probe of the entropy of a system and hence the role of
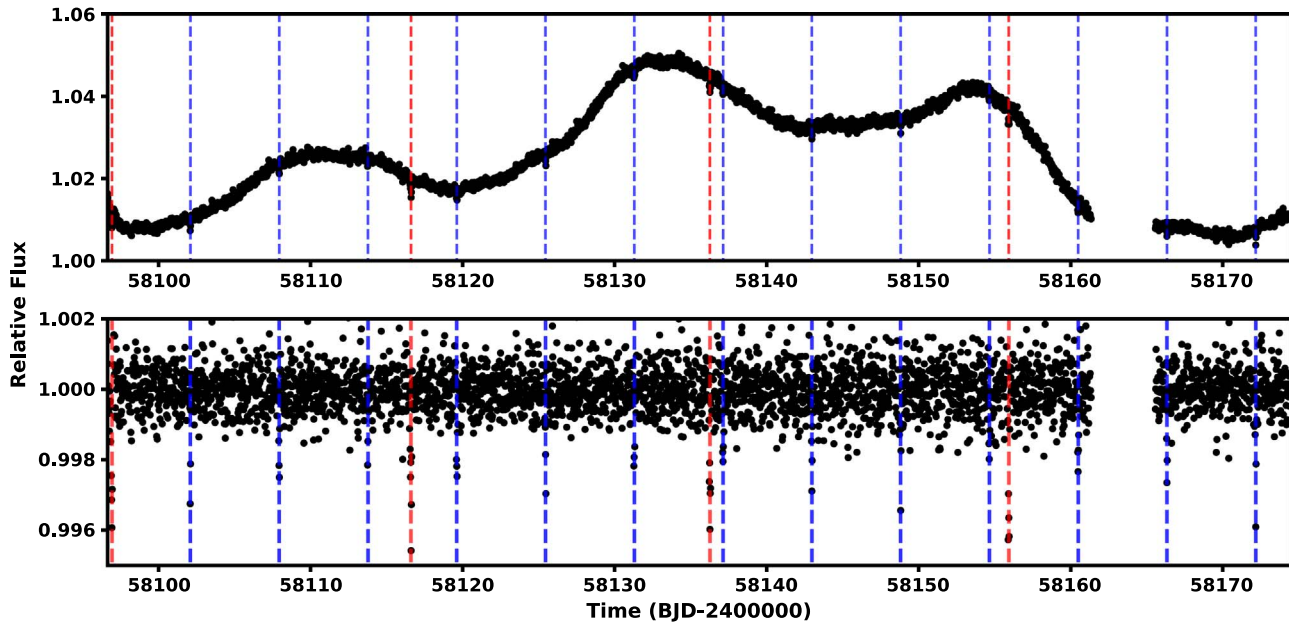

Figure 1. Light curve of K2-264 from *K2* Campaign 16. The top panel shows the light curve after correction of the *K2* roll/flat-field systematic following the method of Vanderburg & Johnson (2014). The lower panel shows the same light curve with the rotational variability removed while the transits were masked (post identification). Red and blue dashed lines indicate the outer (19.66 day) and inner (5.84 day) planets, respectively.

dynamical disruptions from their (expected) initially flat configuration (e.g., Figueira et al. 2012; Ballard & Johnson 2016).

Multi-transiting systems in clusters offer a unique route to study the dynamical properties of planets with known (young) ages. So far, there is only one known multi-transiting system in an open cluster: K2-136, a three-planet system in the 650 Myr old Hyades cluster (Ciardi et al. 2018; Livingston et al. 2018; Mann et al. 2018a). Here, we present the discovery of two planets transiting the 650 Myr old Praesepe cluster star K2-264 (JS 597, EPIC 211964830; Jones & Stauffer 1991) from its *K2* light curve. K2-264 hosts two super-Earth/mini-Neptune-sized planets in short (≈ 6 and ≈ 20 day) period orbits. We describe our discovery and follow-up observations in Section 2, and we describe our analysis to determine stellar properties in Section 3. In Section 4, we place limits on additional planets in the system, and in Sections 5 and 6 we describe our transit fitting to determine stellar parameters and our false positive probability (FPP) analysis. Finally, in Section 7, we discuss the implications from discovering a second multi-transiting cluster system.

2. Observations and Data Reduction

2.1. K2 *Observations and Transit Identification*

K2 observed K2-264 from 2017 December 7 to 2018 February 25 during Campaign 16. The raw pixel level photometry was calibrated using the *Kepler* pipeline (Twicken et al. 2010; Stumpe et al. 2012) prior to public release of the data on 2018 May 30. K2-264 was selected as part of four *K2* guest observer programs in Campaign 16,[9] three of which selected K2-264 on the basis of membership in the Praesepe cluster.

We applied our detrending and transit search pipeline, which is described in detail in Rizzuto et al. (2017), to the data for K2-264. To summarize the process, we first removed the *K2* roll or flat-field systematic, caused by the instability of the *K2* pointing and pixel-response variations using the method of Vanderburg & Johnson (2014). This produced a cleaned light curve that was mostly free of instrumental systematics but still contains signals from stellar variability and transiting planets. We removed the astrophysical variability with a "notch-filter", which fits a 1-day window of the light curve as a combination of an outlier-resistant second-order polynomial and a trapezoidal notch. The inclusion of the notch allows aggressive detrending outside the notch without over-fitting that may remove or weaken transit-like signals. This window is then moved along each point in the light curve, detrending the variability signal from the entire data set. The periodic transits were then identified using the Box Least Squares algorithm (Kovács et al. 2002) on the detrended light curve. Figure 1 shows the rotational variability, detrended light curve, and detected transit signals.

Once the two transiting planets were detected, we re-extracted the data using a simultaneous fit to the *K2* roll systematic, low-frequency stellar variability, and transits, including outlier rejection as described in Vanderburg et al. (2016). The final light curve, following flattening by removal of the best-fit low-frequency variability and significant outliers, was then used for our MCMC transit fitting described below.

2.2. NIR *Spectra from SPEX*

On 2018 June 2, we observed K2-264 with the InfraRed Telescope Facility (IRTF) SpeX medium-resolution spectrograph (Rayner et al. 2003, 2004). We used the 0.″3 slit in SXD mode, which yielded a spectral resolution of $R \simeq 2000$ from 0.7 to 2.55 μm. Extraction and calibration of the spectrum, including flat, bias, and wavelength correction, was carried out using the Spextool package (Cushing et al. 2004), which incorporates the xtellcor package (Vacca et al. 2003) to
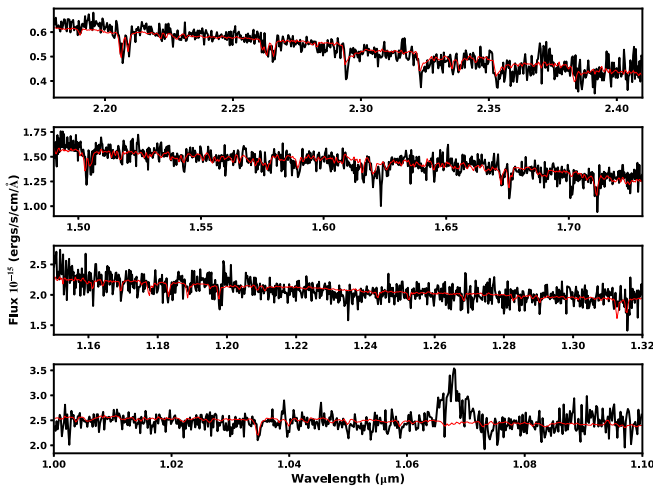
---

[9] GO16022 PI: Rebull, GO16033 PI: Gaudi, GO16052 PI: Stello, GO16060 PI: Agüeros.

Figure 2. Spex NIR spectrum orders of K2-264. The black line shows the reduced data for K2-264, and the red line is an M3 template spectrum for J1142 +2642 taken with the same instrument.

correct for telluric contamination. The observation was taken in poor conditions at high airmass and had a median signal-to-noise ratio (S/N) per pixel of $\simeq$15 in the first two orders covering $1.4-2.5\,\mu$m, and S/N of $\simeq$10 in the two orders covering 0.9–1.3 μm. Given the low S/N of the spectrum, we did not attempt to extract stellar properties such as $T_{\rm eff}$, log g, or metallicity. Figure 2 displays the resulting spectrum of K2-264.

We measured a radial velocity from the spectrum by cross-correlating with a similar spectral-type standard. This was done over each order using the *tellrv* package[10] (Newton et al. 2014). After correcting for Barycentric motion, the cross-correlation yielded a radial velocity for K2-264 of 26 $\pm$ 6 km s^{-1}, which is within $\sim$1σ of the expected expected radial velocity for a Praesepe member.

2.3. Literature Photometry and Astrometry

Photometry from multiple all-sky surveys were compiled to build a full SED for K2-264. Optical *g r i z* magnitudes were taken from the PanSTARRS point source catalog (Flewelling et al. 2016). Near-IR *J*, *H*, and *Ks* photometry was taken from the Two Micron All Sky Survey (2MASS; Skrutskie et al. 2006), the *r'* magnitude was taken from the Carlsberg Meridian Catalog (CMC15; Muiños & Evans 2014). Mid-IR magnitudes in the *W1-4* bands were taken from the *Wide-Field Infrared Survey Explorer* (*WISE*; Wright et al. 2010). K2-264 was not detected in the *W3* and *W4* bands ($\sim$12 and 24 μm) and only upper limits were provided, so we excluded them from our analysis. Proper motions, parallax, and *G*, *RP*, and *BP* magnitudes were taken from the *Gaia* mission second data release (Gaia Collaboration et al. 2018). These data for K2-264 are shown in Table 1.

2.4. Archival Imaging

We examined archival imaging observations of K2-264 from several different surveys to search for nearby stars that might contribute the transit signals we see. In particular, we examined observations from the Palomar Observatory Sky Survey (POSS-

---

Table 1
Properties of the Host Star K2-264

Parameter	Value	Source
	Astrometry	
α R.A.	08 45 26.054	EPIC
δ Decl.	+19 41 54.46	EPIC
μ_α (mas yr^{-1})	-37.900 ± 0.095	*Gaia* DR2
μ_δ (mas yr^{-1})	-13.079 ± 0.061	*Gaia* DR2
π (mas)	5.3598 ± 0.0605	*Gaia* DR2
	Photometry	
G_{Gaia} (mag)	15.6625 ± 0.0006	*Gaia* DR2
BP_{Gaia} (mag)	16.9463 ± 0.006	*Gaia* DR2
RP_{Gaia} (mag)	14.5382 ± 0.0015	*Gaia* DR2
g (mag)	17.259 ± 0.006	PanSTARRS
r (mag)	16.075 ± 0.002	PanSTARRS
i (mag)	14.965 ± 0.003	PanSTARRS
z (mag)	14.471 ± 0.002	PanSTARRS
r (mag)	16.052 ± 0.031	CMC15
J (mag)	13.047 ± 0.025	2MASS
H (mag)	12.386 ± 0.022	2MASS
Ks (mag)	12.183 ± 0.020	2MASS
$W1$ (mag)	12.048 ± 0.023	*WISE*
$W2$ (mag)	11.978 ± 0.023	*WISE*
	Kinematics and Position	
Barycentric RV (km s^{-1})	26 ± 6	This paper
U (km s^{-1})	37.3 ± 4.6	This paper
V (km s^{-1})	-18.0 ± 2.6	This paper
W (km s^{-1})	-14.7 ± 3.5	This paper
X (pc)	139.2 ± 1.6	This paper
Y (pc)	-69.0 ± 0.8	This paper
Z (pc)	103.3 ± 1.2	This paper
Distance (pc)	$186.6^{+2.1}_{-4.1}$	*Gaia* DR2
	Physical Properties	
Rotation Period(days)	22.8 ± 0.6	This paper
Spectral Type	M2.5 $\pm$ 0.5	This paper
$F_{\rm bol}$ (erg cm^{-2} s^{-1})	$(3.068 \pm 0.068) \times 10^{-11}$	This paper
$T_{\rm eff}$ (K)	3580 ± 70	This paper
$M_\star$ ($M_\odot$)	0.471 ± 0.012	This paper
$R_\star$ ($R_\odot$)	0.473 ± 0.014	This paper
$L_\star$ ($L_\odot$)	0.0330 ± 0.0012	This paper
$\rho_\star$ ($\rho_\odot$)	4.5 ± 0.4	This paper
[Fe/H]	0.12 ± 0.04	Praesepe (Boesgaard et al. 2013)

I) to identify background stars at the present-day position of K2-264, and we used observations from the Pan-STARRS survey to search for nearby faint companions.

We first used the POSS images of K2-264 to rule out the presence of bright background stars at the present-day position of the target star. K2-264 was observed by POSS in 1950, when its position was $\sim$2″7 away from its present-day position due to the star's proper motion ($\mu = 40.1 \pm 0.1$ mas yr^{-1}). K2-264's PSF partially overlaps its present-day position, but it is still possible to rule out some nearby companions. Based on nearby stars observed at the same time, we estimate that if there was a background star at the present-day position of K2-264 brighter than $R \sim 19$ mag, we would be able to detect it. Since we see no evidence for such a star, we can rule out the presence of these background
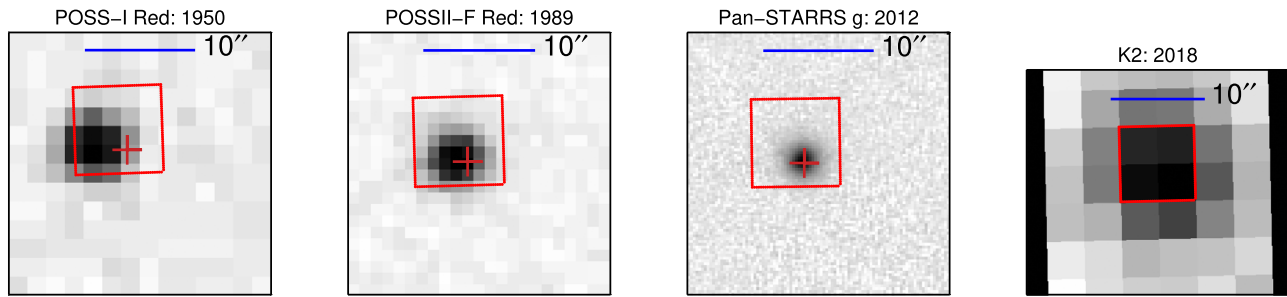
Figure 3. Archival imaging of K2-264, the red cross indicates the present-day position of the target taken from *Gaia* DR2 (Gaia Collaboration et al. 2018), and the red box indicates the *K2* pixels used to make the light curve. Far left: A POSS-I image taken in 1950 of K2-264 on a photographic plate with a red-sensitive emulsion. The star's proper motion has caused its apparent position to move by several arcseconds since 1950, excluding the presence of background contaminants at the present-day position of K2-264. Middle left: A POSS-II image taken in 1989 on a photographic plate with a red-sensitive emulsion. Middle right: An image taken by the Pan-STARRS survey in *g*-band. The higher-resolution and deeper Pan-STARRS images show no signs of nearby stars that might contribute the transit signals we detect toward K2-264. Far right: Summed *K2* image of K2-264.

companions about three magnitudes fainter than K2-264. We show the POSS image in Figure 3.

We also used observations from the Pan-STARRS survey to search for and rule out faint stars near the position of K2-264. Neither a query of the Pan-STARRS archive point source catalog nor visual inspection of images revealed any nearby stars closer to K2-264 than 30″. With Pan-STARRS, we can rule out nearby stars to fairly faint limits ($r \gtrsim 20$). The Pan-STARRS image is shown in Figure 3.

2.5. Companion Constraints from Gaia Data Release 2

While detection limits for additional sources surrounding stars in the *Gaia* second data release (Gaia Collaboration et al. 2018) are not characterized by the *Gaia* team, limits can be estimated using populations of known binaries detected in ground-based imaging surveys. Ziegler et al. (2018a) used a sample of 620 binary companions to *Kepler* Objects of Interest (KOIs) detected with Robo-AO imaging to characterize the detectability of companions 1″–4″ from a primary in the *Gaia* second data release. Ziegler et al. (2018a) find that companions with separations <1 arcsec are not listed as separate sources in the *Gaia* catalog, and provide contrast limits out to separations of 4″.

This method can be extended to smaller separations by examining the quality of the *Gaia* astrometric fit, in particular the significance of the "extra-error" term. In order to do this, we supplemented 363 high-confidence binary companions to KOIs identified by Robo-AO (Law et al. 2014; Baranec et al. 2016; Ziegler et al. 2017, 2018b) with 93 companions detected at $\rho < 1''$ using imaging or aperture mask interferometry with the Near Infrared Camera (NIRC2) on the Keck II telescope by Kraus et al. (2016). The higher spatial resolution of Keck, particularly when combined with aperture masking, provided companions down to $\rho \simeq 10$–20 mas. The Robo-AO LP600 filter is very similar to the *Gaia G* bandpass (Ziegler et al. 2018a), however the companions from Kraus et al. (2016) were detected in *K*-band. Under the assumption that these companions were very likely to be bound due to the small separations, we interpolated *Gaia G* band primary-secondary contrasts using the *K*-band contrast, the primary estimated effective temperature from Kraus et al. (2016), and a 2 Gyr PARSEC 1.2 s isochrone (Chen et al. 2014).

We then queried the *Gaia* second data release (DR2) catalog in a 10 arcsec cone around each KOI with a detected companion. We assessed detection by *Gaia* on the basis of
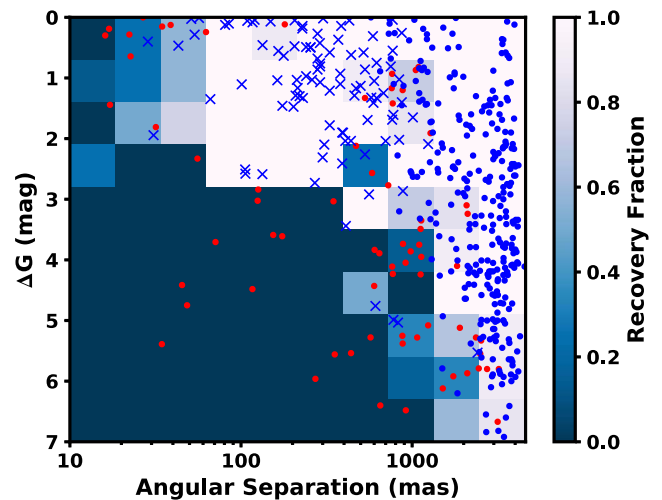

Figure 4. Recovered (blue) and missed (red) known companions to 457 *Kepler* objects of interest from Law et al. (2014), Baranec et al. (2016), Ziegler et al. (2017, 2018b), and Kraus et al. (2016). Red points indicate companions not recovered by *Gaia*, blue crosses indicate astrometrically recovered companions, and blue points indicate companions resolved as separate sources in the *Gaia* DR2 source catalog.

three separate conditions: (1) The companion was identified as a unique source in the catalog at the expected position angle and separation and with the expected contrast (2) The companion was not resolved as a distinct source in the *Gaia* catalog, but the astrometric extra error significance (*D*) was $>10\sigma$. This was only used for companions with separations <1 arcsec. (3) The primary star was missing from the *Gaia* catalog, again this condition was only applied to companions with separations of $\rho < 1''$. Our interpretation assumes that clear binaries where the astrometric solution was extremely poor were removed from the second data release, which is listed in Gaia Collaboration et al. (2018) as the intended operating procedure employed by the *Gaia* data reduction team. Finally, if the contrast of the companion and the magnitude of the primary would indicate a *Gaia G* magnitude of the secondary of >21 mag, we removed that companion from the test sample as it falls below the faint limit for the *Gaia* survey and may not be robustly detected.

Figure 4 displays the separation and contrast of the recovered and non-recovered companions in the *Gaia* second data release. We find similar magnitude limits in the 1–3 arcsec range as
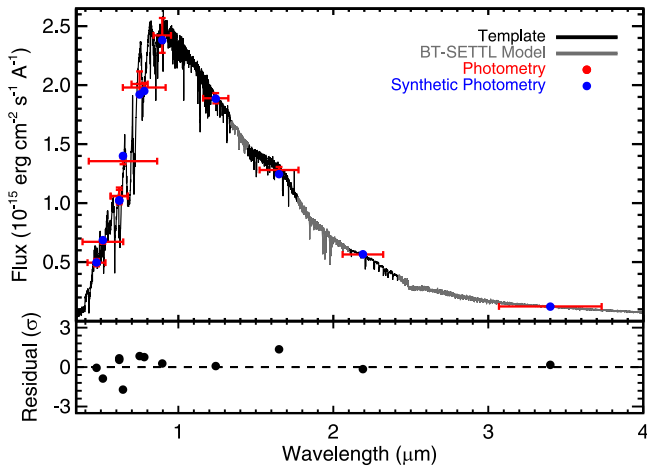
Figure 5. Best-fit spectral template compared to the photometry of K2-264. The template is constructed from observations (black) from Gaidos et al. (2014) with a BT-SETTL model atmosphere of the same temperature interpolated into missing regions of the spectrum (gray). Measured photometry is shown in red, with vertical errors corresponding to the uncertainty in the flux and horizontal error bars showing the FWHM of the filter profile. Blue points mark the synthetic flux measurements derived by convolving the spectrum with the relevant filter profile. The bottom plot shows the difference between the photometry and synthetic photometry in units of standard deviations.

Ziegler et al. (2018a), with 50% recovery for $\Delta G = 3$ mag at 1 arcsec and for $\Delta G = 6$ mag at $3''$. Inside 1 arcsec, companions with $\Delta G < 2$ mag are reliably detected on the basis of the astrometric fit down to separations of 80 mas.

There were no sources within 35 arcsec of K2-264 in *Gaia* DR2, and the astrometric extra error significance for K2-264 is $D = 4.98\sigma$. The *Gaia* DR2 release notes (Gaia Collaboration et al. 2018) state that for stars with well behaved astrometry, D should be considered as a half-normal with mean zero and spread of unity. Furthermore, *Gaia* DR2 astrometry may contain instrument and attitude modeling errors that may inflate the value of D (Gaia Collaboration et al. 2018). A value of $D = 4.98$ is thus not anomalously large considering the number of sources in the *Gaia* catalog. Hence, we can rule out companions with contrasts of less than 2 mag at separations of 80–1000 mas.

3. Stellar Parameters

Effective Temperature and Bolometric Flux: We simultaneously solved for the spectral type and bolometric flux (F_{bol}) by fitting the literature photometry (Section 2.3) using a grid of M-dwarf templates, following the technique outlined in the previous papers in this series (e.g., Mann et al. 2017b, 2018a). For the templates, we used a set of flux-calibrated templates of members of the Hyades open cluster, which were observed as part of programs to characterize nearby M dwarfs (Gaidos et al. 2014). We first filled missing regions of the template spectra for which data were not available with BT-SETTL atmosphere models (Allard et al. 2011) of the corresponding temperature, and then reddened each template according to the $E(B - V)$ value for Praesepe from Taylor (2006). For each template, we computed synthetic magnitudes using the filter profiles and zero-points from Evans et al. (2018),[11] Mann et al. (2015) for other optical bands, and Cohen et al. (2003) for 2MASS. We compared these synthetic magnitudes to the

archival values, letting the template choice and overall flux levels shift as free parameters. For each template, we computed F_{bol} by integrating over the full spectrum. Our final adopted spectral type and F_{bol} were those corresponding to the best-fit template weighted by the χ^2 values from the comparison between observed and synthetic (from the templates) photometry. This method yielded a spectral type of M2.5(±0.5) and and F_{bol} of $(3.068 \pm 0.068) \times 10^{-11}$ erg cm^{-2} s^{-1}. The errors in F_{bol} account for variations due to many possible template fits, uncertainties in the cluster reddening, and uncertainties arising from interpolating over gaps in the spectrum. We show the best-fit template and a comparison to the photometry in Figure 5.

To determine R_*, M_*, and ρ_* we used the empirical M_{K_S}–R_* relation from Mann et al. (2015) and the M_{K_S}–M_* relation from Mann et al. (2018b).[12] We computed M_{K_S} from the *Gaia* distance and 2MASS K_S. This yielded a radius of $0.473 \pm 0.014\,R_\odot$, a mass of $0.471 \pm 0.012\,M_\odot$, and a density of $4.46 \pm 0.40\,\rho_\odot$. We can also assess the accuracy of the radius derived from the M_{K_S}–R_* relation of Mann et al. (2015) using the Stefan–Boltzmann equation, our bolometric flux, temperature of the best-fit template star, and the *Gaia* parallax. We find that the radius corresponding to the best-fit temperature is $0.475 \pm 0.018\,R_\odot$, which agrees with the radius from the M_{K_S}–R_* very closely.

To calculate the total stellar luminosity, we combined our F_{bol} value with the *Gaia* parallax, which yielded $0.0330 \pm 0.0012\,L_\odot$. Joining this with our radius determination and the Stefan–Boltzmann equation produced a T_{eff} of 3580 ± 70 K. This T_{eff} value was consistent with the assigned value for our best-fit template (3560 ± 60 K) derived by comparison to BT-SETTL models (Allard et al. 2011), as described in Mann et al. (2013).

Rotation Period: To determine the rotation period, we took the *K2* roll-corrected light curve prior to removing the stellar variability, masked out the transits from the data, and computed a Lomb–Scargle periodogram spanning periods of 1–40 days. We fit a Gaussian to the largest peak in the periodogram to find the period at the peak power, and conservatively estimate the uncertainty as the standard deviation of the Gaussian divided by the periodogram power. We find the rotation period to be 22.8 ± 0.6 days. The rotation period of K2-264 lies directly on the Praesepe rotation-mass sequence. Figure 6 shows the rotation period of K2-264 in relation to the host stars of the seven other known Praesepe members with transiting planets (Mann et al. 2017b) from *K2* Campaign 5, and the full Praesepe population (Douglas et al. 2017).

Membership in the Praesepe cluster: The kinematics, position, and photometry of K2-264 all place it as a high-confidence member of the Praesepe cluster. Combining our RV measurement for K2-264 with the *Gaia* data release 2 position, proper motions, and parallax measurements allow calculation of the three-dimensional (3D) space velocity to be (U, V, W) = (37.3 ± 4.6, -18.0 ± 2.3, -14.7 ± 3.4) km s^{-1}. This agrees with the 3D space velocity of Praesepe derived from the locus of the known members updated with *Gaia* DR2 astrometry of (42, -20, -10) km s^{-1} with intra-cluster dispersion of 1–2 km s^{-1} (Kraus & Hillenbrand 2007). Figure 7 shows the proper motion offset from the Praesepe velocity projected onto the plane of the sky for K2-264 and the Praesepe

---

[11] Also see Gaia photometric calibration documentation.
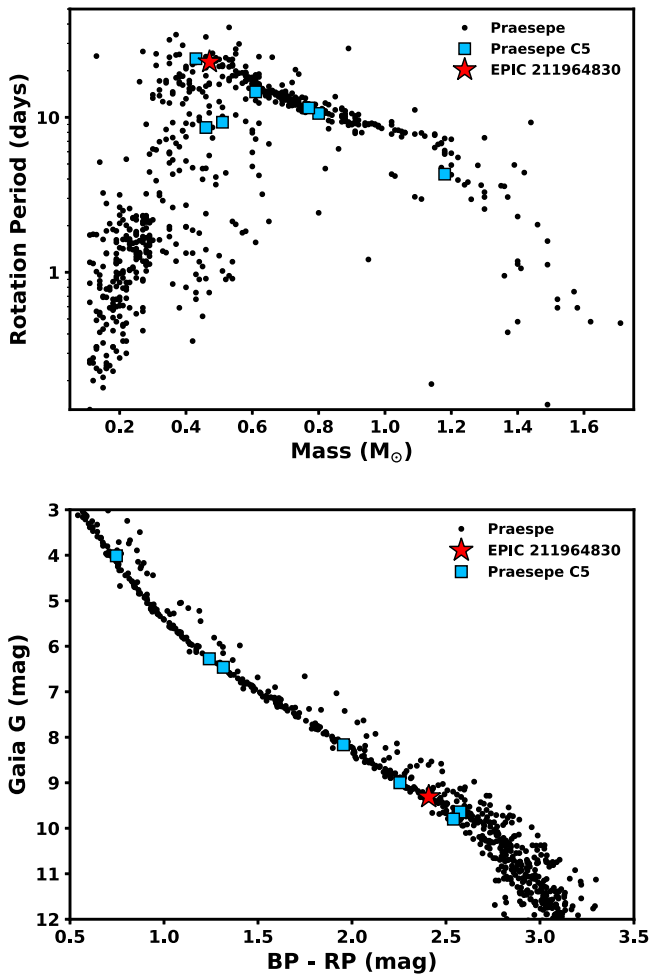
[12] https://github.com/awmann/M_-M_K-

Figure 7. Proper motions offset from the expected cluster motion for K2-264 compared to known Praesepe members from Kraus & Hillenbrand (2007) with membership probability greater than 95%. The intra-cluster dispersion appears to be 1–2 mas yr^{-1}, or equivalently 1–2 km s^{-1}. The proper motion of K2-264 is highly consistent with the projected sky motion of the Praesepe cluster.

narrow single stars sequence rules-out an unresolved companion to K2-264 contributing more that 10%–20% of the total observed flux. This is consistent with the lack of companions with $\Delta G \lesssim 2$ mag determined from the *Gaia* astrometry in Section 2.5.

Metallicity: Given the strong membership of K2-264 in the Praesepe cluster, we can assign the bulk cluster metallicity of the Praesepe population to it. A value of [Fe/H] = 0.12 (Boesgaard et al. 2013) is used when required for other calculations and model fitting.

Figure 6. Top: Rotation periods as a function of estimated stellar mass for Praesepe members from Douglas et al. (2017). The red star indicates the rotation period of K2-264, which closely matches the Praesepe sequence. Bottom: Color–magnitude diagram using *Gaia* DR2 *G*, *RP* and *BP* magnitudes and parallax of Praesepe members from Kraus & Hillenbrand (2007) with membership probabilities greater than 95%. K2-264 (red star) lies on the tight single-star sequence of cluster members. In both panels the blue squares are the host stars of the other seven transiting planets in Praesepe identified in *K2* C5 (Mann et al. 2017b).

members of Kraus & Hillenbrand (2007) with membership probability greater than 95%. Here we take the members from Kraus & Hillenbrand (2007), but plot the de-projected proper motions from *Gaia* DR2. K2-264 falls within the range of the velocity dispersion of the members. The *Gaia* DR2 positions and parallax ($\pi = 5.36 \pm 0.06$ mas; $D = 186.6^{+2.1}_{-4.1}$ pc) place K2-264 on the periphery of the central core of the Praesepe cluster. Figure 8 shows the spatial position slices of known Praesepe members and the position of K2-264 in relation to the cluster. We calculate a kinematic and spatial membership probability of $\sim$97% for K2-264 using the Bayesian membership selection method of Rizzuto et al. (2011, 2015).

In Figure 6, we also show the *Gaia* (*BP-RP*, *G*) color–magnitude diagram of Praesepe members from Kraus & Hillenbrand (2007). The single and binary star sequences are clearly visible, and K2-264 falls directly on the single-star sequence of Praesepe members. In combination with the kinematic and rotational match to the cluster population, this makes membership in Praesepe highly likely. In addition, the
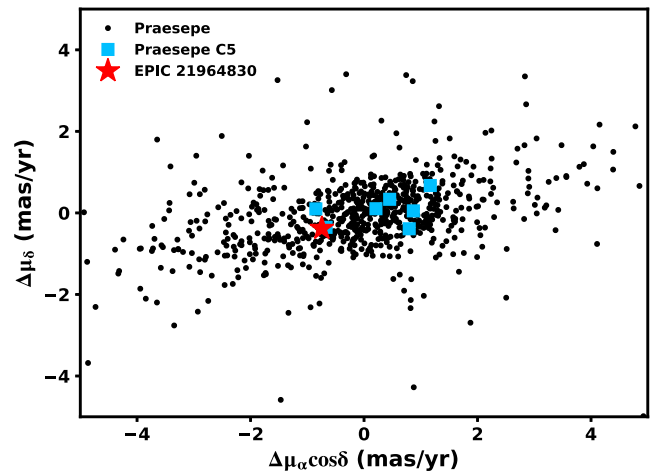
4. Limits on Additional Planets

We tested the sensitivity of the combination of our transit search and detrending pipeline and the *K2* data for K2-264 using the method described in Rizzuto et al. (2017). We injected a series of synthetic planet signals with random parameters into the raw *K2* photometry using the BATMAN model of Kreidberg (2015). We used orbital periods of 1–30 days and planet radii of 0.5–10 $R_{\oplus}$, and allow orbital phase and impact parameter to have values within the interval (0, 1). We fixed the eccentricity to zero in these simulations, as it does not significantly alter detectability of a transit, but would significantly increase the required number of trials to obtain a dense enough mapping of parameter space. We randomly injected 5000 trial planet signals for this test. More information regarding this process can be found in Rizzuto et al. (2017).

For each injected planet, we applied the corrections for the *K2* pointing and stellar variability, and searched for planets using the BLS algorithm, retaining signals with power spectrum peaks of $>7\sigma$. If a planet was detected within 1% of both the injected period and injected orbital phase, we flagged it as recovered. Figure 9 displays the results of the injection-recovery testing. We found that the combination of the *K2* data and our search methodology is sensitive to 1.7 $R_{\oplus}$ planets at orbital periods of 1–10 days, 2.0 $R_{\oplus}$ planets at orbital periods of 10–20 days, and 3.4 $R_{\oplus}$ planets out to periods of 25 days at the 90% recovery level.
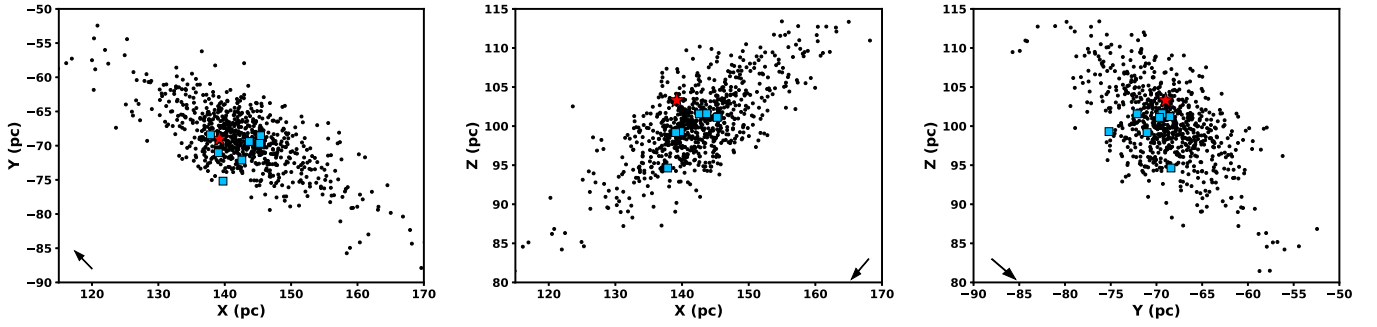
Figure 8. Galactic spatial position of K2-264 (red star) in relation to other Praesepe members (black points) from Kraus & Hillenbrand (2007) with membership probability greater than 95%, computed from *Gaia* DR2 positions and parallaxes. The arrow indicates the typical size and direction of the uncertainty in the positions, which is dominated by the *Gaia* parallax uncertainty. The majority of the objects in front of and behind the core of Praesepe in the line of sight are likely interlopers in the Kraus & Hillenbrand (2007) membership, introduced due to the lack of parallaxes at the time of selection. K2-264 sits on the periphery of the central core of the Praesepe cluster. The blue squares indicate the positions of the host stars of the other seven transiting planets in Praesepe identified in *K2* C5 (Mann et al. 2017b).
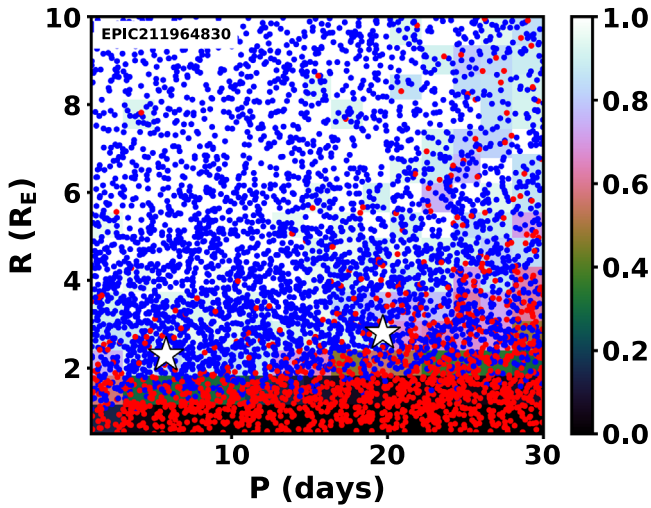
Figure 9. Completeness map for additional planets in the K2-264 system, produced from injection-recovery testing of our search pipeline. Each point represents an injected planet signal, with blue points indicating recovery and red points non-recovery. White stars are the two detected planets b and c. Our pipeline and the *K2* data for K2-264 are sensitive to planets as small as ~1–$2\,R_\oplus$ at orbital periods of 1–20 days.

5. Transit Fitting

To determine transit parameters for K2-264, we fit the cleaned and detrended *K2* light curve with a Markov Chain Monte Carlo (MCMC) as described in Mann et al. (2016a, 2018a) and Johnson et al. (2017). In summary, our MCMC fitting is based on the combination of the BATMAN transit model code (Kreidberg 2015) with the Affine-invariant MCMC code emcee (Foreman-Mackey et al. 2013). The BATMAN transit models were computed including oversampling and binning to the ~30 minute *K2* long-cadence exposures. We implemented a quadratic limb-darkening law, and used the triangular sampling method of Kipping (2013). The free parameters in our model that are different for each planet are the planet–star radius ratio (R_P/R_*), orbital period (P), epoch of first transit mid-point (T_0), impact parameter (b), and two parameters used in place of eccentricity and argument of periastron ($\sqrt{e}\sin\omega$, $\sqrt{e}\cos\omega$). These parameters were all fit simultaneously with a common stellar density (ρ_*) and the limb-darkening parameters (q_1 and q_2).

Table 2
Transit Fit Parameters

Parameter	Planet b	Planet c
Period (days)	$5.839770^{+0.000063}_{-0.000061}$	$19.663650^{+0.000303}_{-0.000306}$
R_P/R_*	$0.0439^{+0.0036}_{-0.0026}$	$0.0536^{+0.0035}_{-0.0027}$
T_0 (BJD-2400000)	$58102.09356^{+0.00046}_{-0.00046}$	$58096.93729^{+0.00077}_{-0.00071}$
Impact Parameter	$0.44^{+0.29}_{-0.28}$	$0.37^{+0.30}_{-0.25}$
Duration[a] (hr)	$1.88^{+0.17}_{-0.39}$	$2.92^{+0.20}_{-0.50}$
Inclination[a] (degrees)	$88.9^{+0.7}_{-0.7}$	$89.6^{+0.3}_{-0.3}$
a/R_*[a]	$22.4^{+0.7}_{-0.7}$	$50.4^{+1.6}_{-1.5}$
Eccentricity[b]	<0.50	<0.45
R_P[c] ($R_\oplus$)	$2.27^{+0.20}_{-0.16}$	$2.77^{+0.20}_{-0.18}$
$T_{\rm eq}$[c] (K)	489^{+12}_{-13}	326^{+8}_{-9}

Global Parameters	
ρ_* ($\rho_\odot$)	$4.45^{+0.39}_{-0.40}$
u_1	$0.42^{+0.09}_{-0.09}$
u_2	$0.27^{+0.08}_{-0.08}$

Notes.
[a] Inclination, ω, a/R_* and transit duration were not fit as part of our MCMC but were derived from other fit parameters (see Section 5).
[b] The most likely eccentricities for both systems is ~0, and so we report only the 1σ upper limit.
[c] R_P $T_{\rm eq}$ were calculated using $T_{\rm eff}$ from Section (3). Equilibrium temperature $T_{\rm eq}$ was calculated assuming an albedo of 0.3.

We applied a Gaussian prior on stellar density ρ_*, determined from our SED fitting described in Section 3. We also applied a Gaussian prior of the limb-darkening parameters determined from the Limb Darkening Tool Kit (LDTK; Parviainen & Aigrain 2015) using the Husser et al. (2013) models, the *Kepler* filter response function, and the stellar parameters from Section 3. The priors computed were 0.42 ± 0.10 and 0.38 ± 0.05 for u_1 and u_2, respectively. The Gaussian prior was applied after conversion to the triangular sampling parameterization for quadratic limb darkening of Kipping (2013). All other parameters were explored with uniform priors with physical boundaries (e.g., $0 < b < 1$). We ran the MCMC chain for 200,000 steps, with 50000 steps of burn-in.

The transit fit parameters and other derived quantities are reported in Table 2. For each value, we report the median, with errors derived from the 16th and 84th percentile values from
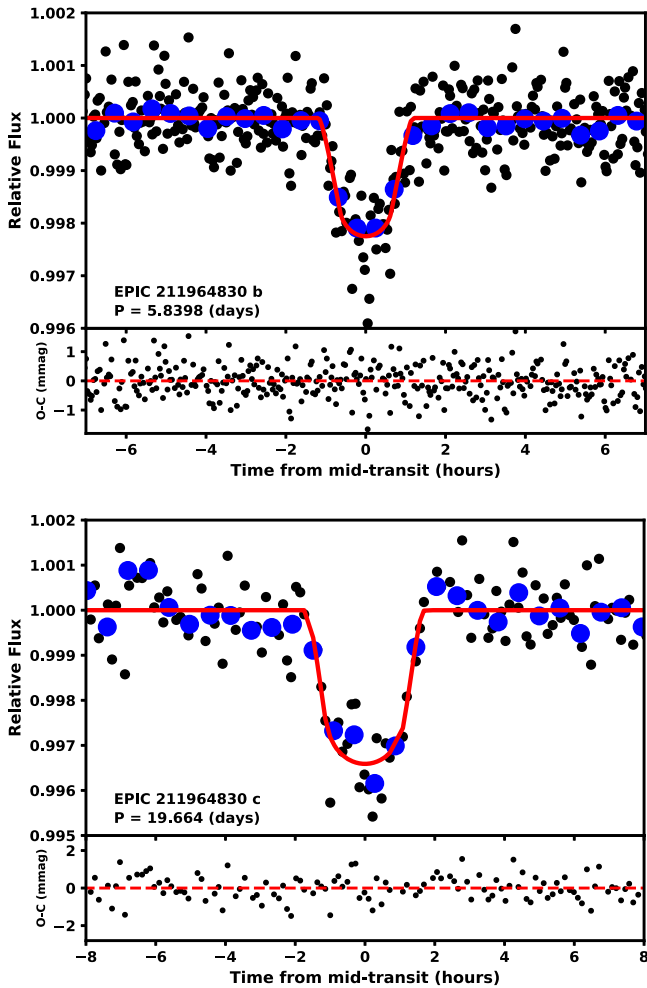
Figure 10. Phase-folded light curves centered on the transits for the two detected planets, with best-fit models from our MCMC transit fitting. The black points are the *K2* observations, the blue circles are the binned data, and the red line is the best-fit transit model generated with BaTMAN (Kreidberg 2015). The lower panel in each figure shows the best-fit residuals.

our fit posteriors. The best-fit transit models are shown in Figure 10. We also show posterior distributions for a subset of parameters (R_p/R_*, e, b, ρ_*) in Figure 11.

Both planets have most likely eccentricities close to zero, which is expected for multiple systems of short-period planets, though both the eccentricity and impact parameters for the planets are not well-constrained by the *K2* data. Both planets are also similar in size with radii of $2.27^{+0.20}_{-0.16}\,R_\oplus$ and $2.77^{+0.20}_{-0.18}\,R_\oplus$.

6. False Positive Probability

While most planet candidates detected by *Kepler* and *K2* are likely to be *bona fide* exoplanets, some transit-like signals may be caused by other astrophysical scenarios. We quantified the likelihood of one of these scenarios causing either of the two transit signals we see toward K2-264 using the open-source vespa software package (Morton 2015). Vespa calculates the FPP of transiting signals using the procedure described by Morton (2012) and Morton et al. (2016). In particular, vespa performs a Bayesian model comparison between several different scenarios which might cause transit-like signals (transiting planets, an eclipsing binary on the target star, an

eclipsing binary on a physically bound companion star, or an eclipsing binary on an unassociated background star), and using the transit light curve, stellar parameters, photometric measurements, and observational constraints, determines the likelihood of each model.

In the case of K2-264, we ran vespa using the transit light curve, broadband photometric measurements from the 2MASS survey,[13] and constraints on the presence of nearby stars from the 2MASS *J*-band image of K2-264.[14] Based on these inputs, vespa calculated an FPP of 4×10^{-3} for K2-264 b and 9×10^{-4} for K2-264 c. These FPPs do not take into account the fact that candidates in multi-candidate systems are considerably less likely to be false positives than candidates in single-candidate systems (Latham et al. 2011; Lissauer et al. 2012). We take this into account by applying a "multiplicity boost" to the calculated FPPs for K2-264 b and c. Following Lissauer et al. (2012), we divide the calculated FPP for K2-264 b and c by a factor of 25 as K2-264 is a two-candidate system. This agrees with the value derived by Sinukoff et al. (2016) for *K2* data. After applying the multiplicity boost, we find FPPs for K2-264 b and c of about 10^{-4} and 4×10^{-5}, respectively. Based on these very low FPPs, we consider both candidates in the K2-264 system to be validated planets.

7. Discussion

We have reported the discovery and characterization of a two-planet transiting system in the Praesepe open cluster. There are now several detected transiting planets in young open clusters and associations observed by *K2*, though K2-264 is one of only two multiple-planet systems, the other being K2-136, a three transiting-planet system in the Hyades open cluster (Mann et al. 2018a).

K2-264 b and c are both likely mini-Neptunes, and both sit near the upper envelope of the field mass–planet radius distribution, as is seen for other planets in intermediate-age clusters. These two planets continue the trend of young open clusters M dwarfs hosting planets of larger radii than have been observed for planets transiting older field population dwarfs from the original *Kepler* sample (Dressing & Charbonneau 2015; Mann et al. 2017b). Figure 12 shows the planet radii and host star masses of the M-dwarf hosted young planets identified in the ZEIT survey (Mann et al. 2016a, 2016b, 2017b, 2018a), including K2-264 b/c, compared to older transiting systems. The possible inflation in radii at ∼650 Myr may be a sign of ongoing atmosphere loss (e.g., Lopez et al. 2012). With further completeness testing on the entire sample of Hyades and Praesepe stars observed by *K2* a measure of the rate and significance of the potential radius difference could be measured.

Systems with multiple transiting planets offer the potential for many science cases not possible with single transit systems. In particular, eccentricity and stellar density can strongly constraint each other (Van Eylen & Albrecht 2015; Mann et al. 2017a). Planet masses for multiple systems can also be measured from TTV's (Hadden & Lithwick 2017). Though we

---

[13] Previous studies have found that vespa produces more reliable results when the broadband photometry used in its FPP calculations only comes from one photometric survey (such as the *Kepler* Input Catalog or the 2MASS survey, Shporer et al. 2017; Mayo et al. 2018).

[14] We calculated a "contrast curve" by fitting a simple (Moffat function) PSF model to the image of K2-264, subtracting the PSF model away, and calculating the 3σ upper limit on the brightness of stars in the residual image.
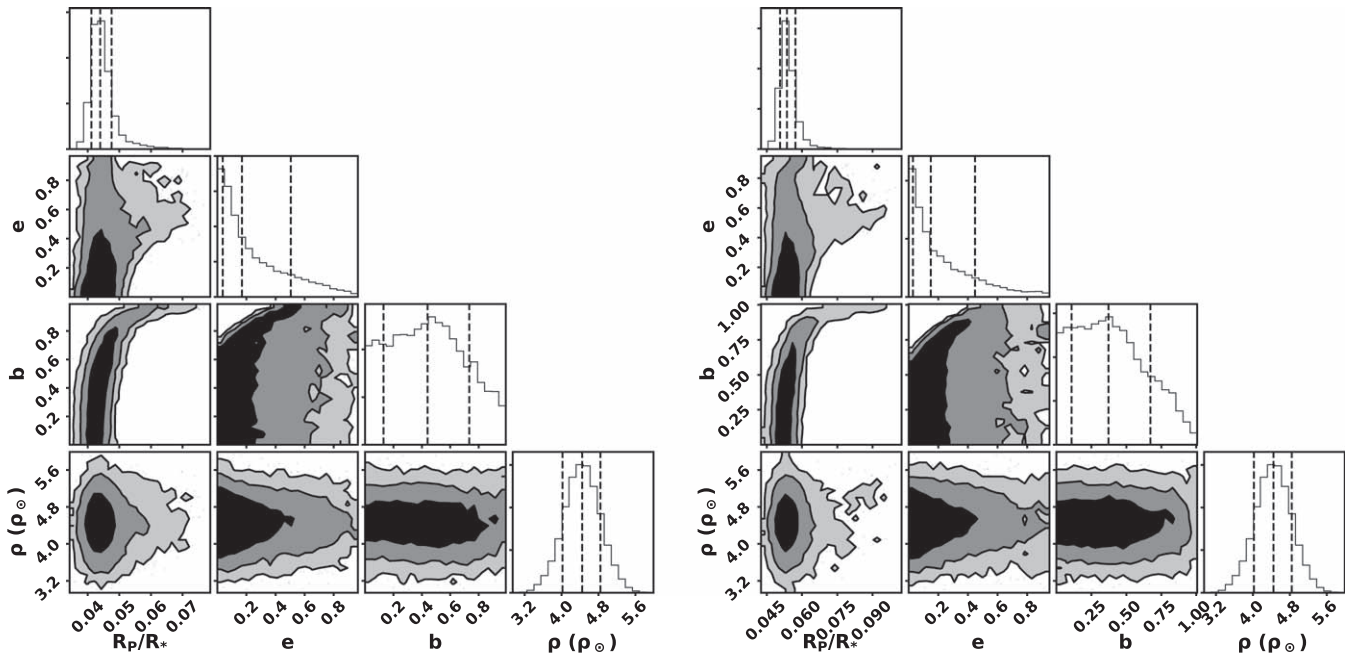
Figure 11. Posteriors for a subset of transit parameters from our MCMC fitting for the inner (left) and outer (right) planets orbiting K2-264. The shaded regions show the 68%, 95%, and 99.7% confidence regions, and the dashed lines show the 16th, 50th, and 84th percentiles, respectively.
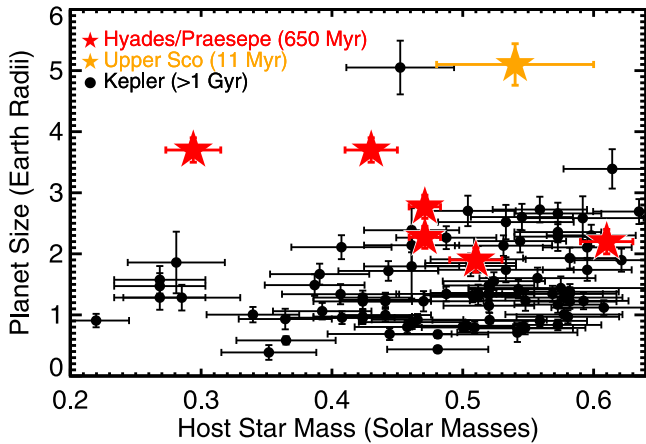

Figure 12. Host star mass and planet radii for the seven transiting planetary systems in Praesepe and the Hyades from *K2* C4/5 (Mann et al. 2016a, 2017b, 2018a) and those presented in this paper from C16, compared to older M-dwarf hosted planets from the original *Kepler* samples (Dressing & Charbonneau 2015). The 650 Myr Praesepe and Hyades planet population have larger radii than those hosted by older M dwarfs. The single 10 Myr old planet in Upper Scorpius (K2-33 b; Mann et al. 2016b) is also significantly larger than the older planets.

did not explicitly test for TTV's, the detection of TTV's in the *K2* data set is unlikely; similar size planets show variations of <15 minutes, which is smaller than the long-cadence timing of ≃30 minutes. In particular, TTV's on planet b due to planet c are expected to be very small (<1 minute) given that the orbital periods are very far from a resonance (Agol et al. 2005). One scenario where TTV detection could be possible involves the presence of a third planet in or near e.g., a 2:1 resonance with the inner planet b. Such a planet would have to be approximately earth-mass to have avoided detection in the *K2* light curve. The TTV amplitude from such a planet on the ephemeris of K2-264 b, assuming zero eccentricities, is

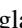5–15 minutes depending on the proximity to resonance (Agol et al. 2005).
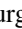
The currently available long-cadence data from *K2* is particularly unsuited to the science cases described above. However, K2-264 is highly amenable to follow-up photometry. Both planets are large enough that ground-based facilities could resolve their transits (≃3 mmag), though the faintness of the host star (r ≃ 16 mag) may be prohibitive for small apertures at high cadence. Shorter cadence data resolving ingress and egress shapes can place stronger constraints on eccentricity, and offer suggestions as to the types of formation mechanisms responsible for forming these two short-period planets. Space-based follow-up with the *Hubble Space Telescope* or *Spitzer* is possible for both planets. In *Spitzer* channel 1 (≃3.5 μm; Hora et al. 2008), K2-264 is ≃12 mag (Wright et al. 2010) and in a 2 minutes exposure an S/N of 500 ppm is possible. This is sufficient to resolve the transit shape from even a single transit.

Follow-up spectroscopy to measure the masses of K2-264 b, c may not be possible. K2-264 shows stellar variability with a period 22.8 days and photometric amplitude of ≃3%. If the star is seen equator-on, this amplitude of variability is expected to produce RV variability of ≃30 m s^{-1} in a similar band as *K2*. Using the mass–radius relation for planets from Weiss & Marcy (2014) and the radii inferred from our transit fitting, we find that K2-264 b, c have likely masses of 5.8 $M_\oplus$ and 7 $M_\oplus$, respectively. Assuming circular orbits and the stellar properties derived above, these masses correspond to radial velocity semi-amplitudes of 3.4 m s^{-1} and 2.7 m s^{-1}, respectively. The amplitude of these signals is significantly smaller than the expected stellar rotations signal. Moving to the near-infrared, where the stellar variability is expected to have significantly smaller amplitude, could alleviate this problem in combination with our prior knowledge of the rotation period of the star.

ORCID iDs

Aaron C. Rizzuto ⓘ https://orcid.org/0000-0001-9982-1332
Andrew Vanderburg ⓘ https://orcid.org/0000-0001-7246-5438
Andrew W. Mann ⓘ https://orcid.org/0000-0003-3654-1602
Adam L. Kraus ⓘ https://orcid.org/0000-0001-9811-568X
Courtney D. Dressing ⓘ https://orcid.org/0000-0001-8189-0233
Marcel A. Agüeros ⓘ https://orcid.org/0000-0001-7077-3664
Stephanie T. Douglas ⓘ https://orcid.org/0000-0001-7371-2832

References

Adams, F. C., & Laughlin, G. 2006, ApJ, 649, 1004
Agol, E., Steffen, J., Sari, R., & Clarkson, W. 2005, MNRAS, 359, 567
Allard, F., Homeier, D., & Freytag, B. 2011, in ASP Conf. Ser. 448, 16th Cambridge Workshop on Cool Stars, Stellar Systems, and the Sun, ed. C. Johns-Krull, M. K. Browning, & A. A. West (San Francisco, CA: ASP), 91
Ballard, S., & Johnson, J. A. 2016, ApJ, 816, 66
Baranec, C., Ziegler, C., Law, N. M., et al. 2016, AJ, 152, 18
Boesgaard, A. M., Roper, B. W., & Lum, M. G. 2013, ApJ, 775, 58
Borucki, W. J., Koch, D., Basri, G., et al. 2010, Sci, 327, 977
Cai, M. X., Portegies Zwart, S., & van Elteren, A. 2018, MNRAS, 474, 5114
Chatterjee, S., Ford, E. B., Matsumura, S., & Rasio, F. A. 2008, ApJ, 686, 580
Chen, Y., Girardi, L., Bressan, A., et al. 2014, MNRAS, 444, 2525
Ciardi, D. R., Crossfield, I. J. M., Feinstein, A. D., et al. 2018, AJ, 155, 10

Cloutier, R., & Lin, M.-K. 2013, MNRAS, 434, 621
Cohen, M., Wheaton, W. A., & Megeath, S. T. 2003, AJ, 126, 1090
Cushing, M. C., Vacca, W. D., & Rayner, J. T. 2004, PASP, 116, 362
Dahm, S. E. 2015, ApJ, 813, 108
David, T. J., Hillenbrand, L. A., Petigura, E. A., et al. 2016, Natur, 534, 658
Deck, K. M., & Agol, E. 2015, ApJ, 802, 116
Deck, K. M., & Agol, E. 2016, ApJ, 821, 96
Douglas, S. T., Agüeros, M. A., Covey, K. R., & Kraus, A. 2017, ApJ, 842, 83
Dressing, C. D., & Charbonneau, D. 2015, ApJ, 807, 45
Ehrenreich, D., Bourrier, V., Wheatley, P. J., et al. 2015, Natur, 522, 459
Evans, D. W., Riello, M., De Angeli, F., et al. 2018, A&A, 616, A4
Figueira, P., Marmier, M., Boué, G., et al. 2012, A&A, 541, A139
Flewelling, H. A., Magnier, E. A., Chambers, K. C., et al. 2016, arXiv:1612.05243
Foreman-Mackey, D., Hogg, D. W., Lang, D., & Goodman, J. 2013, PASP, 125, 306
Gaia Collaboration, Brown, A. G. A., Vallenari, A., et al. 2018, arXiv:1804.09365
Gaidos, E., Anderson, D. R., Lépine, S., et al. 2014, MNRAS, 437, 3133
Gillon, M., Triaud, A. H. M. J., Demory, B.-O., et al. 2017, Natur, 542, 456
Hadden, S., & Lithwick, Y. 2017, AJ, 154, 5
Hora, J. L., Carey, S., Surace, J., et al. 2008, PASP, 120, 1233
Howell, S. B., Sobeck, C., Haas, M., et al. 2014, PASP, 126, 398
Husser, T.-O., Wende-von Berg, S., Dreizler, S., et al. 2013, A&A, 553, A6
Inamdar, N. K., & Schlichting, H. E. 2016, ApJL, 817, L13
Johnson, M. C., Cochran, W. D., Addison, B. C., Tinney, C. G., & Wright, D. J. 2017, AJ, 154, 137
Jones, B. F., & Stauffer, J. R. 1991, AJ, 102, 1080
Kipping, D. M. 2013, MNRAS, 435, 2152
Kipping, D. M., Dunn, W. R., Jasinski, J. M., & Manthri, V. P. 2012, MNRAS, 421, 1166
Kovács, G., Zucker, S., & Mazeh, T. 2002, A&A, 391, 369
Kraus, A. L., Herczeg, G. J., Rizzuto, A. C., et al. 2017, ApJ, 838, 150
Kraus, A. L., & Hillenbrand, L. A. 2007, AJ, 134, 2340
Kraus, A. L., Ireland, M. J., Huber, D., Mann, A. W., & Dupuy, T. J. 2016, AJ, 152, 8
Kreidberg, L. 2015, PASP, 127, 1161
Latham, D. W., Rowe, J. F., Quinn, S. N., et al. 2011, ApJL, 732, L24
Law, N. M., Morton, T., Baranec, C., et al. 2014, ApJ, 791, 35
Lissauer, J. J., Dawson, R. I., & Tremaine, S. 2014, Natur, 513, 336
Lissauer, J. J., Marcy, G. W., Rowe, J. F., et al. 2012, ApJ, 750, 112
Livingston, J. H., Dai, F., Hirano, T., et al. 2018, AJ, 155, 115
Lopez, E. D., Fortney, J. J., & Miller, N. 2012, ApJ, 761, 59
Mann, A. W., Dupuy, T., Muirhead, P. S., et al. 2017a, AJ, 153, 267
Mann, A. W., Feiden, G. A., Gaidos, E., Boyajian, T., & von Braun, K. 2015, ApJ, 804, 64
Mann, A. W., Gaidos, E., & Ansdell, M. 2013, ApJ, 779, 188
Mann, A. W., Gaidos, E., & Gaudi, B. S. 2010, ApJ, 719, 1454
Mann, A. W., Gaidos, E., Mace, G. N., et al. 2016a, ApJ, 818, 46
Mann, A. W., Gaidos, E., Vanderburg, A., et al. 2017b, AJ, 153, 64
Mann, A. W., Newton, E. R., Rizzuto, A. C., et al. 2016b, AJ, 152, 61
Mann, A. W., Vanderburg, A., Rizzuto, A. C., et al. 2018a, AJ, 155, 4
Mann, C., Tellesbo, C. A., Bromely, B. C., & Kenyon, S. J. 2018b, AJ, in press
Martín, E. L., Lodieu, N., Pavlenko, Y., & Béjar, V. J. S. 2018, ApJ, 856, 40
Mayo, A. W., Vanderburg, A., Latham, D. W., et al. 2018, AJ, 155, 136
Morton, T. D. 2012, ApJ, 761, 6
Morton, T. D. 2015, VESPA: False positive probabilities calculator, Astrophysics Source Code Library, ascl:1503.011
Morton, T. D., Bryson, S. T., Coughlin, J. L., et al. 2016, ApJ, 822, 86
Muiños, J. L., & Evans, D. W. 2014, AN, 335, 367
Newton, E. R., Charbonneau, D., Irwin, J., et al. 2014, AJ, 147, 20
Obermeier, C., Henning, T., Schlieder, J. E., et al. 2016, AJ, 152, 223
Parviainen, H., & Aigrain, S. 2015, MNRAS, 453, 3821
Pecaut, M. J., Mamajek, E. E., & Bubar, E. J. 2012, ApJ, 746, 154
Pepper, J., Gillen, E., Parviainen, H., et al. 2017, AJ, 153, 177
Rayner, J. T., Onaka, P. M., Cushing, M. C., & Vacca, W. D. 2004, Proc. SPIE, 5492, 1498
Rayner, J. T., Toomey, D. W., Onaka, P. M., et al. 2003, PASP, 115, 362
Rizzuto, A. C., Ireland, M. J., & Kraus, A. L. 2015, MNRAS, 448, 2737
Rizzuto, A. C., Ireland, M. J., & Robertson, J. G. 2011, MNRAS, 416, 3108
Rizzuto, A. C., Mann, A. W., Vanderburg, A., Kraus, A. L., & Covey, K. R. 2017, AJ, 154, 224
Shporer, A., Zhou, G., Vanderburg, A., et al. 2017, ApJL, 847, L18

Sinukoff, E., Howard, A. W., Petigura, E. A., et al. 2016, ApJ, 827, 78
Skrutskie, M. F., Cutri, R. M., Stiening, R., et al. 2006, AJ, 131, 1163
Stumpe, M. C., Smith, J. C., Van Cleve, J. E., et al. 2012, PASP, 124, 985
Taylor, B. J. 2006, AJ, 132, 2453
Thompson, S. E., Coughlin, J. L., Hoffman, K., et al. 2018, ApJS, 235, 38
Twicken, J. D., Chandrasekaran, H., Jenkins, J. M., et al. 2010, Proc. SPIE, 7740, 77401U
Vacca, W. D., Cushing, M. C., & Rayner, J. T. 2003, PASP, 115, 389
Van Cleve, J. E., Howell, S. B., Smith, J. C., et al. 2016, PASP, 128, 075002

Vanderburg, A., & Johnson, J. A. 2014, PASP, 126, 948
Vanderburg, A., Latham, D. W., Buchhave, L. A., et al. 2016, ApJS, 222, 14
Vanderburg, A., Mann, A. W., Rizzuto, A., et al. 2018, AJ, 156, 46
Van Eylen, V., & Albrecht, S. 2015, ApJ, 808, 126
Weiss, L. M., & Marcy, G. W. 2014, ApJL, 783, L6
Wright, E. L., Eisenhardt, P. R. M., Mainzer, A. K., et al. 2010, AJ, 140, 1868
Ziegler, C., Law, N. M., Baranec, C., et al. 2018a, arXiv:1806.10142
Ziegler, C., Law, N. M., Baranec, C., et al. 2018b, AJ, 155, 161
Ziegler, C., Law, N. M., Morton, T., et al. 2017, AJ, 153, 66